Creation of Superheterojunction Polymers via Direct Polycondensation: Segregated and Bicontinuous Donor−Acceptor π-Columnar Arrays in Covalent Organic Frameworks for Long-Lived Charge Separation

Shangbin Jin,[†] Mustafa Supur,[⊥] Matthew Addicoat,[‡] Ko Furukawa,[§] Long Chen,[†,¶] Toshikazu Nakamura,[†] Shunichi Fukuzumi,*[,⊥] Stephan Irle,*[,‡] and Donglin Jiang*[,†]

[†]Department of Materials Molecular Science, Institute for Molecular Science, National Institutes of Natural Sciences, 5-1 Higashiyama, Myodaiji, Okazaki, Aichi 444-8787, Japan

[¶]College of Materials Science and Engineering, Beijing Institute of Technology, Zhongguancun south street 5, Beijing 100081, China

[⊥]Department of Material and Life Science, Graduate School of Engineering, Osaka University, ALCA, JST, 2-1 Yamadaoka, Suita, Osaka 565-0871, Japan

[§]Institute for Research Promotion Center for Instrumental Analysis, Niigata University, 8050 Ikarashi, 2 Nocho, Niigata, Niigata 950-2181, Japan

[‡]WPI-Research Initiative-Institute of Transformative Bio-Molecules and Department of Chemistry, Graduate School of Science, Nagoya University, Furo-cho, Chikusa-ku, Nagoya, Aichi 464-8602, Japan

S *Supporting Information*

ABSTRACT: By developing metallophthalocyanines and diimides as electron-donating and -accepting building blocks, herein, we report the construction of new electron donor−acceptor covalent organic frameworks (COFs) with periodically ordered electron donor and acceptor π-columnar arrays via direct polycondensation reactions. X-ray diffraction measurements in conjunction with structural simulations resolved that the resulting frameworks consist of metallophthalocyanine and diimide columns, which are ordered in a segregated yet bicontinuous manner to form built-in periodic π-arrays. In the frameworks, each metallophthalocyanine donor and diimide acceptor units are exactly linked and interfaced, leading to the generation of superheterojunctions—a new type of heterojunction machinery, for photoinduced electron transfer and charge separation. We show that this polycondensation method is widely applicable to various metallophthalocyanines and diimides as demonstrated by the combination of copper, nickel, and zinc phthalocyanine donors with pyrommellitic diimide, naphthalene diimide, and perylene diimide acceptors. By using time-resolved transient absorption spectroscopy and electron spin resonance, we demonstrated that the COFs enable long-lived charge separation, whereas the metal species, the class of acceptors, and the local geometry between donor and acceptor units play roles in determining the photochemical dynamics. The results provide insights into photoelectric COFs and demonstrate their enormous potential for charge separation and photoenergy conversions.
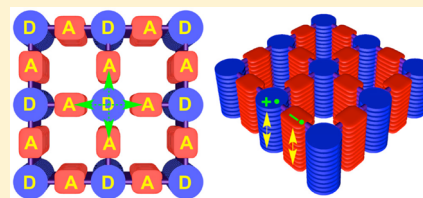
1. INTRODUCTION

Covalent organic frameworks (COFs) are an emerging class of crystalline porous polymers that allow atomically precise integration of organic building blocks into periodic structures.[1−12] By virtue of their unique structural features, COFs have shown great potential in a variety of applications, ranging from gas storage to semicoductors, catalysis, and photoenergy conversion.[2−12] The development of π-units as building blocks enables the construction of two-dimensional (2D) COFs in which π-units are linked and stacked to form periodic π-columnar arrays. This concept has led to the finding of various new organic semiconductors with periodic π-arrays.[2,5b−k,6] Those studies demonstrated that COFs could offer a powerful platform for creating next-generation organic π-electronic structures with built-in π-orderings upon polycondensation.

An open question is that is it possible to form electron donor and acceptor COFs with ordered donor-on-donor and acceptor-on-acceptor π-columnar structures upon direct copolymerization; the creation of such segregated yet bicontinuous donor−acceptor structures is vital to next-generation devices for photoinduced charge separation and photoenergy conversion. Self-assembly of donor−acceptor systems into bicontinuous arrays and organization of donor−acceptor units in amorphous porous organic polymers have been previously reported.[13] In addition to those systems, we have developed the direct polycondensation of electron donor and acceptor monomers to form donor−acceptor COFs in which electron donor and acceptor units are covalently linked

Chart 1. Schematic Representation of the Donor−Acceptor COFs (D$_{MPc}$−A$_{DI}$-COFs) with Covalently Linked Phthalocyanine-diimide (MPc-DI) Structures[a]
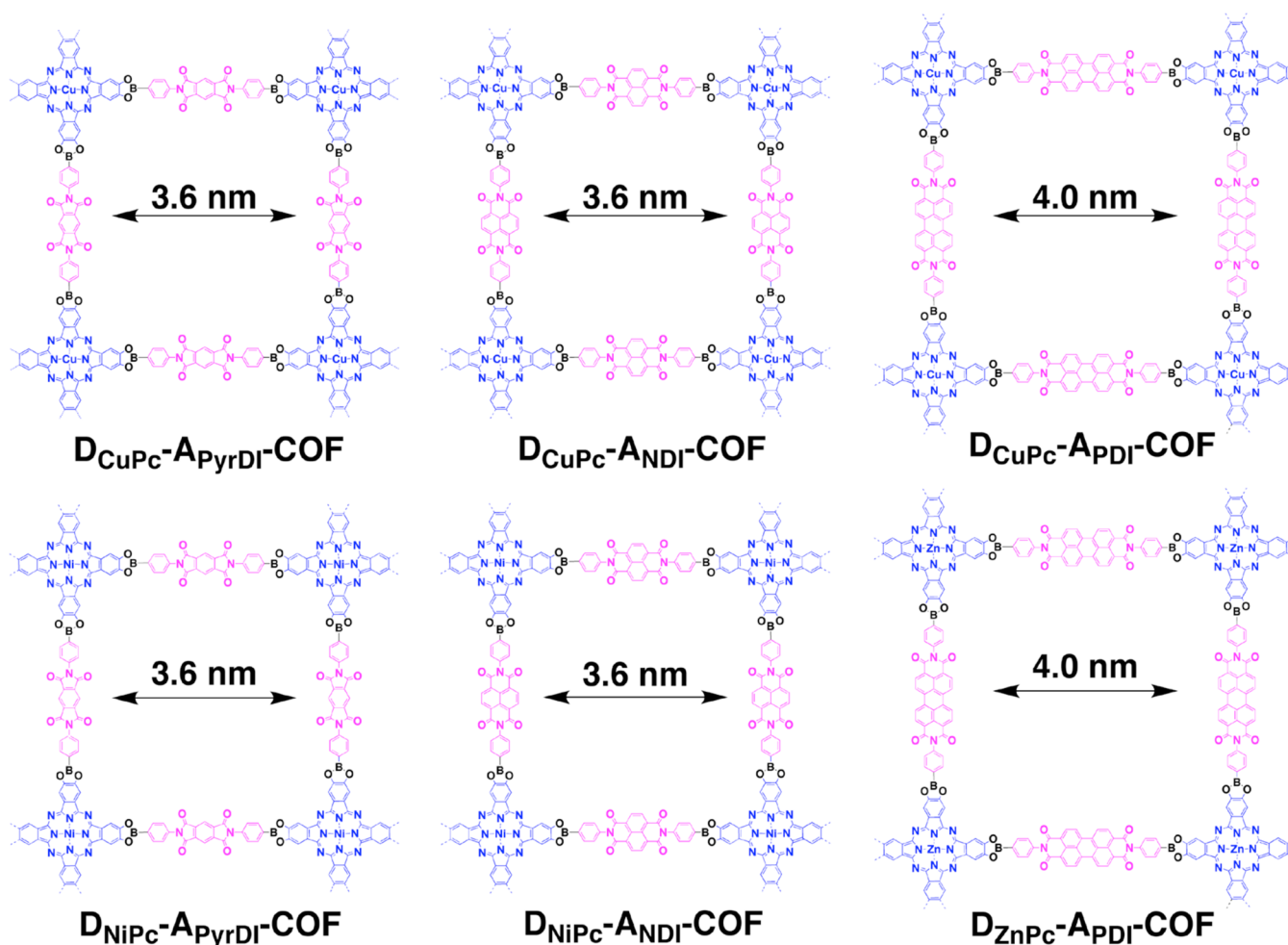
[a]Metallophthalocyanines are highlighted in blue, and diimides are in red. CuPc, NiPc, and ZnPc represent copper(II), nickel(II), and zinc(II) phthalocyanine donors, whereas PyrDI, NDI, and PDI represent pyrommellitic diimide, naphthalene diimide, and perylene diimide acceptors, respectively. MPc units occupy the vertices, and DI blocks locate the edges of the tetragonal polygon sheets that further stack to form layered segregated bicontinuous π-arrays with periodically ordering structures.

and stacked into bicontinuous π-structures.[2] Recently, we[5k] and Bein[6] have developed the utilization of donor−acceptor COFs as photoactive layers for photoenergy conversion. However, electron donor−acceptor COFs have been limited to only a few examples; the development of new building blocks and COF structures are highly desired for developing long-lived charge separation and energy conversion materials.

In this study, we focused on developing π-building blocks for the construction of new donor−acceptor COFs and elucidated their unique characters in photoinduced electron transfer and charge separation. We employed electron-donating metallophthalocyanines and electron-accepting diimide derivatives as the building blocks for the synthesis of new COFs and constructed photofunctional COFs with built-in donor−acceptor segregated bicontinuous structures (Chart 1, D$_{MPc}$−A$_{DI}$-COFs). We resolved crystal structures by using X-ray diffraction (XRD) measurements in conjunction with molecular and electronic structure calculations, elucidated their photochemical events and charge dynamics by using time-resolved transient absorption spectroscopy and electron spin resonance spectroscopy, and correlated their structure−function relationships. We demonstrated that the segregated bicontinuous

columnar π-arrays, found in donor−acceptor COFs features in each metallophthalocyanine donor and diimide acceptor unit, are exactly linked and interfaced, leading to the generation of superheterojunctions—a new mechanism that enables photoinduced electron transfer and long-lived charge separation.

2. RESULTS AND DISCUSSION

2.1. Synthesis and Characterization of D$_{MPc}$−A$_{DI}$-COFs.
D$_{MPc}$−A$_{DI}$-COFs were newly synthesized through the direct polycondensation of (2,3,9,10,16,17,23,24-octahydroxy phthalocyaninato) copper(II) (CuPc[OH]$_8$), (2,3,9,10,16,17,23,24-octahydroxy phthalocyaninato) nickel(II) (NiPc[OH]$_8$), or (2,3,9,10,16,17,23,24-octahydroxy phthalocyaninato) zinc(II) (ZnPc[OH]$_8$) with N,N′-di(4-boronophenyl)-pyrommellitic-1,2,4,5-tetracarboxylic acid diimide (PyrDIDA), N,N′-di(4-boronophenyl)-naphthalene-1,4,5,8-tetracarboxylic acid diimide (NDIDA), or N,N′-di(4-boronophenyl)-perylene-1,6,7,12-tetracarboxylic acid diimide (PDIDA) under solvothermal conditions (Supporting Information, SI). We tuned the reaction conditions, including solvent, reaction temperature, and reaction time, with an aim to preparing highly crystalline COFs. We found that a mixture of anhydrous N,N-
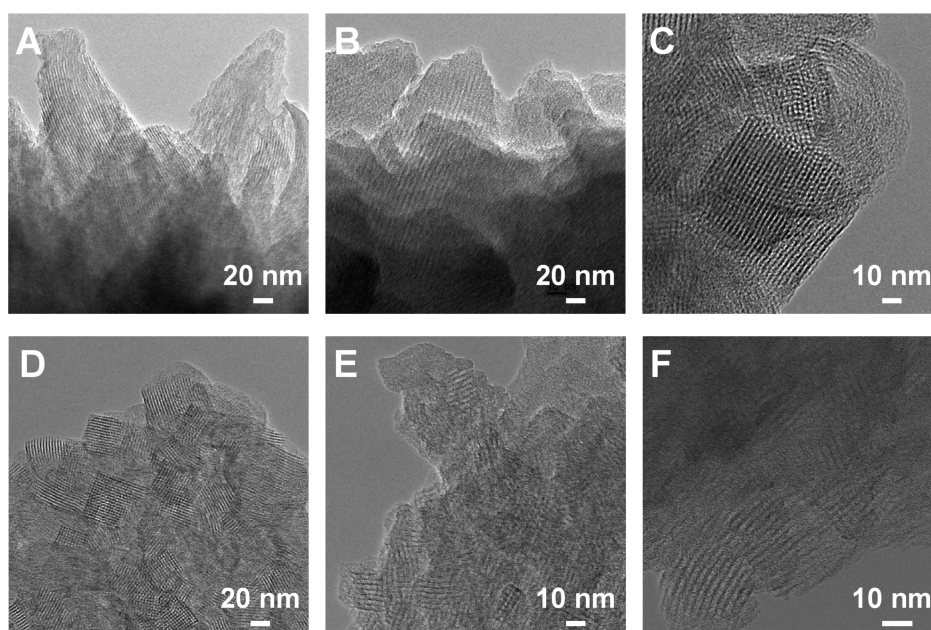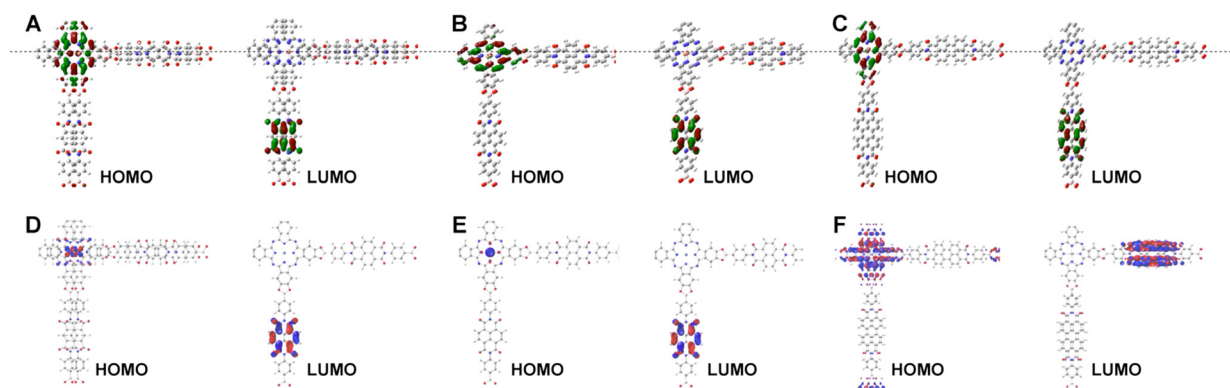
Figure 1. HR-TEM images (A) D_{CuPc}-A_{PyrDI}-COF, (B) D_{NiPc}-A_{PyrDI}-COF, (C) D_{CuPc}-A_{NDI}-COF, (D) D_{NiPc}-A_{NDI}-COF, (E) D_{CuPc}-A_{PDI}-COF, and (F) D_{ZnPc}-A_{PDI}-COF.

Table 1. DFTB Calculations of Monolayer and Stacked Layers of D_{MPc}-A_{DI}-COFs

COFs	stacking mode	$a = b$ (Å)	c (Å)	slipped distance (Å)	twisted angle (deg)	LJ dispersion energy (kcal mol^{-1})	total crystal stacking energy per unit cell (kcal mol^{-1})
D_{CuPc}-A_{PyrDI}	monolayer	35.7	−	−	0	0.8166	−
	eclipsed AA		3.49	−		1.2479	109.87
	slipped AA		3.33	2.1	0	1.2607	122.02
	staggered AB		3.30	−		1.4991	34.54
D_{CuPc}-A_{NDI}	monolayer	36.2	−	−	0	0.9113	−
	eclipsed AA		3.48	−		1.3922	123.24
	slipped AA		3.53	0.4	20	1.3869	154.72
	staggered AB		3.31	−		1.6349	53.53
D_{CuPc}-A_{PDI}	monolayer	40.3	−	−	20	1.0976	−
	eclipsed AA		3.54	−		1.6788	158.69
	slipped AA		3.53	0.4	15	1.6797	158.79
	staggered AB		3.31	−		1.9558	71.87
D_{NiPc}-A_{PyrDI}	monolayer	35.7	−	−	0	0.8152	−
	eclipsed AA		3.49	−		1.2459	110.33
	slipped AA		3.37	1.65	0	1.2473	119.98
	staggered AB		3.34	−		1.4975	33.49
D_{NiPc}-A_{NDI}	monolayer	36.0	−	−	20	0.9008	−
	eclipsed AA		3.55	−		1.3837	128.66
	slipped AA		3.55	0.0	15	1.3860	130.30
	staggered AB		3.32	−		1.6016	56.20
D_{ZnPc}-A_{PDI}	monolayer	40.4	−	−	20	1.0965	−
	eclipsed AA		3.55	−		1.6784	159.26
	slipped AA		3.53	0.0	15	1.6904	164.34
	staggered AB		3.31	−		1.9513	71.96

dimethylacetamide (DMAc) and o-dichlorobenzene (o-DCB) in a volume ratio of 2/1 or 4/1 generated crystalline COFs with prominent XRD signals. Reaction of $MPc[OH]_8$ with PyrDIDA or NDIDA requires 3 days, whereas the condensation with PDIDA in relation to its poor solubility needs a longer reaction time of 7 days. A typical protocol is as follows: a mixture of DMAc/o-DCB (2 mL, 2/1 by vol.), DIDA (0.02 mmol), and $MPc[OH]_8$ (0.01 mmol) in a 10 mL Pyrex tube was sonicated for 1 min, degassed through three freeze−pump−thaw cycles, sealed under vacuum, and kept at 120 °C for 3 or 7 days. The

Figure 2. HOMO−LUMO maps of (A) D_{CuPc}-A_{PyrDI}-COF, (B) D_{CuPc}-A_{NDI}-COF, (C) D_{CuPc}-A_{PDI}-COF, (D) D_{NiPc}-A_{PyrDI}-COF, (E) D_{NiPc}-A_{NDI}-COF, and (F) D_{ZnPc}-A_{PDI}-COF in their stacked structures.

precipitate was collected by centrifugation, washed with dehydrated DMAc until the solution was colorless, washed with dehydrated acetone for 3 times, and dried under 120 °C overnight, to yield D_{MPc}-A_{DI}-COF as dark green or red solids. Accordingly, D_{CuPc}-A_{PyrDI}-COF, D_{NiPc}-A_{PyrDI}-COF, D_{CuPc}-A_{NDI}-COF, D_{NiPc}-A_{NDI}-COF, D_{CuPc}-A_{PDI}-COF, and D_{ZnPc}-A_{PDI}-COF were prepared as dark green or red solids in isolated yields of 59%, 67%, 62%, 61%, 63%, and 59%, respectively.

Elemental analysis of D_{MPc}-A_{DI}-COFs revealed that the C, N, and H contents are consistent with the theoretical values for infinite 2D polymer sheets (Table S1 in SI). Infrared spectroscopy confirmed the formation of boronate linkages in the COFs, as evidenced by characteristic vibration bands at 1348 and 1083 cm^{-1}, which are assignable to the B−O and C−B bonds, respectively (Figure S1 in SI). Field emission scanning electron microscopy revealed that D_{MPc}-A_{DI}-COFs assume particle or belt shapes with size ranged from hundreds nanometer to several micrometer scales (Figure S2 in SI). High-resolution transmission electron microscopy (HR-TEM) showed the presence of porous textures (Figure 1).

2.2. Structural Simulations. The density-functional tight-binding (DFTB) method including Lennard-Jones (LJ) dispersion was used to simulate the optimum structures of the D_{MPc}-A_{DI}-COFs (Table 1). First the series of D_{CuPc}-A_{DI}-COFs with CuPc donor and PyrDI, NDI, and PDI acceptors was optimized. The electronic configuration of the copper(II) atom is $[Ar]3d,^9$ and thus each monolayer unit cell has one unpaired spin ($S = 1/2$). In each bilayer model, these spins may be paired or unpaired. In order to determine the relative energy of unrestricted $S = 0$ and 1 bilayer structures, two-dimensional periodic boundary condition (PBC) calculations, employing the Γ-point approximation, were undertaken on the DFTB optimized geometries of the monolayer and lowest energy stacked structure. Calculations employed the PBE0 density functional and the STO-3G basis set.

For the monolayer structures of D_{CuPc}-A_{DI}-COFs, the obtained optimal cell lengths are $a = b = 35.7$, 36.2, and 40.3 Å for the PyrDI, NDI, and PDI acceptors, respectively (Table 1). The monolayers with NDI and PyrDI acceptors remain planar, however, the H−H repulsion in the PDI linker causes twist, which, in turn, prompts the phenyl group to counter-tilt, leaving a dihedral angle of 20° relative to the CuPc plane. Using these optimal monolayer structures, three stacked configurations, AA, slipped AA, and staggered AB, were generated and optimized. For the slipped-AA configuration, several initial geometries were created by shifting the second layer in 0.1 Å

increments along either the a axis or both the a and b axes, and all structures thus created were allowed to relax without constraints.

In the stacked frameworks, D_{CuPc}-A_{PyrDI}-COF adopts a planar conformation with an interlayer distance (c) of 3.33 Å, where the neighboring sheets are slipped along the a axis by 1.9 Å. This optimal structure gives rise to a total crystal stacking energy per unit cell of 122.0 kcal mol^{-1} for D_{CuPc}-A_{PyrDI}-COF (Table 1). For D_{CuPc}-A_{NDI}-COF and D_{CuPc}-A_{PDI}-COF, the minimum energy structure is slipped by 0.4 Å along the a and b axes and holds an interlayer distance (c) of 3.53 Å. The total crystal stacking energies per unit cell are 154.72 and 158.79 kcal mol^{-1} for D_{CuPc}-A_{NDI}-COF and D_{CuPc}-A_{PDI}-COF, respectively. These two COFs exhibit similar geometries, where the diimide linker twists rather than remaining planar and the phenyl group is tilted with respect to the CuPc plane by 20 and 15° for NDI and PDI, respectively. The driving force behind the non-planarity of these COFs is likely to be the formation of interlayer hydrogen bonds between the diimide oxygen and phenyl hydrogen atoms. In the minimum energy D_{CuPc}-A_{PDI}-COF structure, the interlayer O···H distance is 2.33 Å, which is 2.40 Å for D_{CuPc}-A_{NDI}-COF. These interlayer O···H distances are within the hydrogen-bonding distance.

Based on the optimized layer structures, for the series of D_{CuPc}-A_{DI}-COFs, the singly occupied molecular orbitals (SOMO) are centered on the CuPc units (Figure 2). On the other hand, the LUMO is centered on the diimide acceptor in the cases of D_{CuPc}-A_{NDI}-COFs and D_{CuPc}-A_{PDI}-COF. However, for D_{CuPc}-A_{PyrDI}-COF, the LUMO and LUMO+1 resemble the SOMO, and the LUMO+2 is centered on the PyrDI acceptor. The D_{CuP}-A_{DI}-COFs adopt a high-spin state in the layered structure.

The molecular and electronic structures of stacked isomers of the analogous structures D_{NiPc}-A_{PyrDI}-COF, D_{NiPc}-A_{NDI}-COF, and D_{ZnPc}-A_{PDI}-COF were also optimized. For the monolayer structures, the obtained optimal cell lengths are $a = b = 35.7$, 36.0, and 40.4 Å for D_{NiPc}-A_{PyrDI}-COF, D_{NiPc}-A_{NDI}-COF, and D_{ZnPc}-A_{PDI}-COF, respectively (Table 1). The PyrDI linker remains planar, whereas the phenyl groups on the NDI and PDI units twist 20° relative to the MPc plane. As with the CuPc COFs, AA, slipped AA, and staggered AB stacked configurations were generated from each monolayer and optimized. For the slipped AA configuration, the degree of slip was again scanned in 0.1 Å increments along either the a axis or both the a and b axes, and all structures thus created were allowed to relax without constraints. For the D_{NiPc}-A_{PyrDI}-COF system, the

minimum energy structure is the slipped AA stacking structure with an interlayer distance of 3.38 Å and a planar conformation. D_{NiPc}-A_{PyrDI}-COF has a total crystal stacking energy of 112.0 kcal mol^{-1}.

For both D_{NiPc}-A_{NDI}-COF and D_{ZnPc}-A_{PDI}-COF, the minimum energy structure is a slipped AA stacking structures with a slip of 1.65 Å along the *a* axis. The total crystal stacking energies per unit cell per layer are 130.3 and 164.3 kcal mol^{-1}, whereas the corresponding interlayer distances are 3.55 and 3.53 Å for D_{NiPc}-A_{NDI}-COF and D_{ZnPc}-A_{PDI}-COF, respectively. Both COFs exhibit similar geometries, whereas the diimide units twist rather than remaining planar, and the phenyl group is tilted by 15° with respect to the MPc plane. These twisted NDI and PDI units enable the formation of interlayer hydrogen bonds between the diimide oxygen and the phenyl hydrogen atoms. The HOMOs are centered, in each case, on the MPc units, and the LUMOs are delocalized on the diimide moieties in the layered structures (Figure 2).

The above calculations reveal that the optimal structures of D_{MPc}-A_{DI}-COFs are dependent on the central metal species and the acceptor units. Especially, the acceptor units play a vital role in determining the twist angles and the total crystal stacking energy. A general tendency is that the COFs with larger acceptor π systems possess higher total crystal stacking energy, despite not remaining planar (Table 1). In this sense, PDI is superior to NDI and PyrDI units. The NDI and PDI units allow interlayer hydrogen-bonding interactions, in addition to the interlayer π−π forces, thus leading to exceptional crystal stacking energy of the COFs.

2.3. Crystalline Structures of D_{MPc}-A_{DI}-COFs. The crystalline structures of D_{MPc}-A_{DI}-COFs were resolved by the XRD measurements in conjunction with Pawley refinements and the above DFTB structural simulations. Depending on acceptors, we categorized the six members of D_{MPc}-A_{DI}-COFs into three classes: (1) D_{CuPc}-A_{PyrDI}-COF and D_{NiPc}-A_{PyrDI}-COF; (2) D_{CuPc}-A_{NDI}-COF and D_{NiPc}-A_{NDI}-COF; and (3) D_{CuPc}-A_{PDI}-COF and D_{ZnPc}-A_{PDI}-COF.

For class 1, D_{CuPc}-A_{PyrDI}-COF (Figure 3A, red curve) and D_{NiPc}-A_{PyrDI}-COF (purple curve) exhibited XRD peaks at 2.48, 5.04, 7.62, 10.18, and 12.66°, which were assigned to the (100), (200), (300), (400), and (500) facets, respectively. The appearance of XRD peaks at 26.1° (inset), which is attributed to the (001) facets with an interlayer distance of 3.4 Å, indicates that D_{CuPc}-A_{PyrDI}-COF and D_{NiPc}-A_{PyrDI}-COF have periodic structure along the layered direction. Pawley refinements (green curves) reproduced the experimentally observed XRD pattern with a negligible difference (black curves), confirming the correctness of the above peak assignments. XRD pattern simulations using the slipped AA structure generated a profile (blue curve), which reproduced the position and intensity of experimentally observed XRD patterns well. On the other hand, the staggered AB mode gave rise to an XRD pattern (brown curve) that could not reproduce the experimentally observed XRD profiles.

For class 2, D_{CuPc}-A_{NDI}-COF (Figure 3B, red curve) and D_{NiPc}-A_{NDI}-COF (purple curve) exhibited XRD signals at 2.44, 4.94 to 7.42, 9.92, and 12.44°, which were assigned to the (100), (200), (300), (400), and (500) facets, respectively. The presence of (001) facet at 26.0° (inset) indicates that the 2D polygon layers are ordered to stack at an interval of 3.4 Å. Pawley refinements (green curves) reproduced the XRD patterns with negligible difference (black curves), indicating that the above assignments of the XRD peaks are correct. One
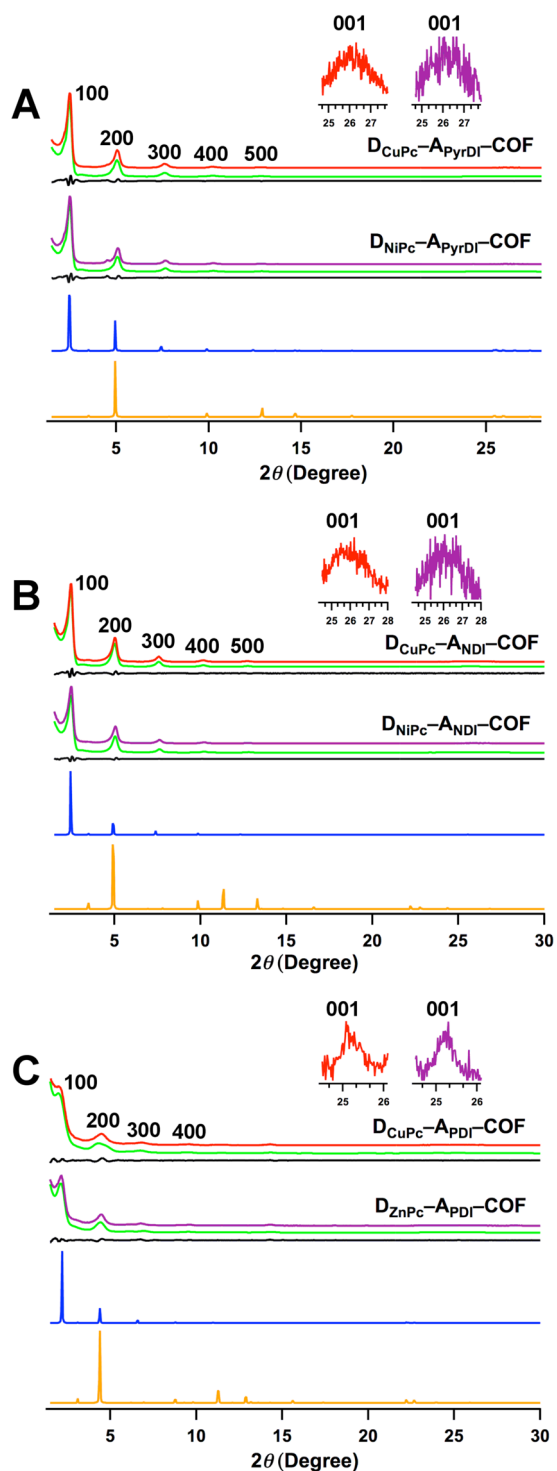
Figure 3. Powder XRD of D_{MPc}-A_{DI}-COFs. Experimental XRD of (A) D_{CuPc}-A_{PyrDI}-COF (red) and D_{NiPc}-A_{PyrDI}-COF (purple); (B) D_{CuPc}-A_{NDI}-COF (red) and D_{NiPc}-A_{NDI}-COF (purple); and (C) D_{CuPc}-A_{PDI}-COF (red) and D_{ZnPc}-A_{PDI}-COF (purple). The blue curves and brown curves are the simulated slipped AA stacking structures and simulated AB stacking structures.

may notice that the lattice sizes of D_{CuPc}-A_{NDI}-COF and D_{NiPc}-A_{NDI}-COF are slightly larger than those of D_{CuPc}-A_{PyrDI}-COF and D_{NiPc}-A_{PyrDI}-COF. XRD pattern simulations using the slipped AA mode (blue curve) reproduced the experimentally observed data, whereas the staggered AB mode (brown curve) did not reproduce the data.
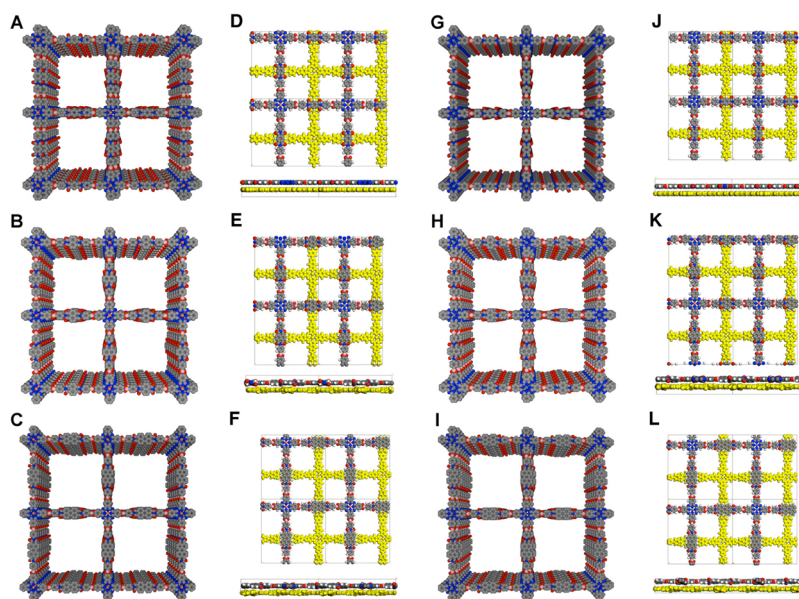
Figure 4. AA stacking structures of (A) D_{CuPc}-A_{PyrDI}-COF, (B) D_{CuPc}-A_{NDI}-COF, (C) D_{CuPc}-A_{PDI}-COF, (G) D_{NiPc}-A_{PyrDI}-COF, (H) D_{NiPc}-A_{NDI}-COF, and (I) D_{ZnPc}-A_{PDI}-COF. Staggered AB stacking structures of (D) D_{CuPc}-A_{PyrDI}-COF, (E) D_{CuPc}-A_{NDI}-COF, (F) D_{CuPc}-A_{PDI}-COF, (J) D_{NiPc}-A_{PyrDI}-COF, (K) D_{NiPc}-A_{NDI}-COF, and (L) D_{ZnPc}-A_{PDI}-COF (top and side views are shown).

D_{CuPc}-A_{PDI}-COF (Figure 3C, red curve) and D_{ZnPc}-A_{PDI}-COF (purple curve) consist of the largest lattice size among the series. Their XRD peaks appeared at 2.12, 4.46, 6.76, 9.56, and 25.3°, which are assigned to the (100), (200), (300), (400), and (001) facets, respectively. The assignment of these XRD signals was confirmed by Pawley refinement (green curves), which exhibited negligible difference (black curves) from the experimentally observed XRD patterns. The twist angle between the phenyl of PDI units and MPc planes is 20° and 15° for monolayer and slipped AA stacking layer structure, which indicates that the $\pi-\pi$ interaction between 2D layers decreases the twist angle significantly. XRD simulations also indicate that the slipped AA stacking structure (blue curve) reproduced the experimentally observed profiles. In contrast, the staggered AB structure could not reproduce the measured profiles.

The above results of crystal structure resolution indicate that D_{MPc}-A_{DI}-COFs assume slipped AA stacking structures, which give rise to periodically aligned donor−acceptor heterojunctions (Figure 4). This donor−acceptor configuration constitutes not only periodically ordered donor and acceptor arrays but also 1D nanopores. The staggered AB mode gives rise to overlapped nanopores (Figure 4).

2.4. Porosity. As elucidated by the crystal structures, D_{MPc}-A_{DI}-COFs consists of open 1D nanopores. Their porosity was investigated by nitrogen adsorption measurements at 77 K. All the samples exhibited type IV sorption curves (Figure 5), which are characteristics of mesoporous materials. D_{CuPc}-A_{PyrDI}-COF (Figure 5A) and D_{NiPc}-A_{PyrDI}-COF (Figure 5B) exhibited Brunauer−Emmitt−Teller (BET) surface areas of 1357 and 1172 m^2 g^{-1}, respectively, whereas their pore volumes are 1.13 and 0.95 cm^3 g^{-1}, respectively. The pore size distribution profiles (Figure 5G, H) were deduced from the sorption isotherm curves and exhibited only one kind of mesopore, which accounts for the porosity of the COFs. The BET surface area and pore volume of D_{CuPc}-A_{NDI}-COF (Figure 5C) were 1726 m^2 g^{-1} and 1.46 cm^3 g^{-1}, respectively, whereas D_{NiPc}-A_{NDI}-COF (Figure 5D) exhibited the BET surface area and

pore volume of 1432 m^2 g^{-1} and 1.15 cm^3 g^{-1}, respectively. Similarly, the pore size distribution profiles (Figure 5I,J) revealed the presence of only one kind of mesopore with the size that is consistent with the theoretical calculated one.

The BET surface areas of D_{CuPc}-A_{PDI}-COF (Figure 5E) and D_{ZnPc}-A_{PDI}-COF (Figure 5F) were determined to be 414 and 519 m^2 g^{-1}, respectively, whereas their pore volumes were 0.48 and 0.55 cm^3 g^{-1}, respectively. The pore size distribution profiles (Figure 5K,L) indicate that only one kind of mesopore exists in the two COFs. These porosity results indicate that condensation of metallophthalocyanine units with diimide derivatives allows the synthesis of crystalline porous COFs with bicontinuous and segregated donor and acceptor columns and open 1D mesoporous channels.

2.5. Solid-State Electronic Absorption. To evaluate light absorption functions and ground-state interaction between donor and acceptor units in COFs, the solid samples of D_{MPc}-A_{DI}-COFs were utilized for electronic absorption spectroscopic measurements (K/M spectra). Solid samples of CuPc, NiPc, and ZnPc exhibited B-bands at 425, 420, and 433 nm, respectively, accompanied by their strong Q bands appeared at 687, 625, and 684 nm, respectively (Figure S4, SI). On the other hand, PyrDI, NDI, and PDI exhibited absorption in the range of 250−448, 300−430, and 380−610 nm with their peak tops at 303, 386, and 496 nm, respectively (Figure S3, SI).

Compared with the monomers, D_{MPc}-A_{DI}-COFs exhibited several features in their absorption spectra (Figure 6). (1) The B-bands of D_{MPc}-A_{DI}-COFs were blue-shifted from those of the corresponding MPc monomers (Figure 6, dotted black curves). For example, D_{CuPc}-A_{NDI}-COF exhibited a blue shift of 30 nm from 425 to 395 nm (Figure 6A, blue curve). D_{NiPc}-A_{PyrDI}-COF and D_{NiPc}-A_{NDI}-COF exhibited blue shifts from 425 nm to 420 and 392 nm, respectively (Figure 6B, green and blue curves). D_{ZnPc}-A_{PDI}-COF exhibited the most significant blue shift from 433 to 379 nm (Figure 6C, green curve). These blue shifts are consistent with H-type aggregation of the MPc π-planes, as indicated by the Kasha principle.[14] (2) The absorption bands contributed to the imide units were red-shifted in D_{MPc}-A_{DI}-
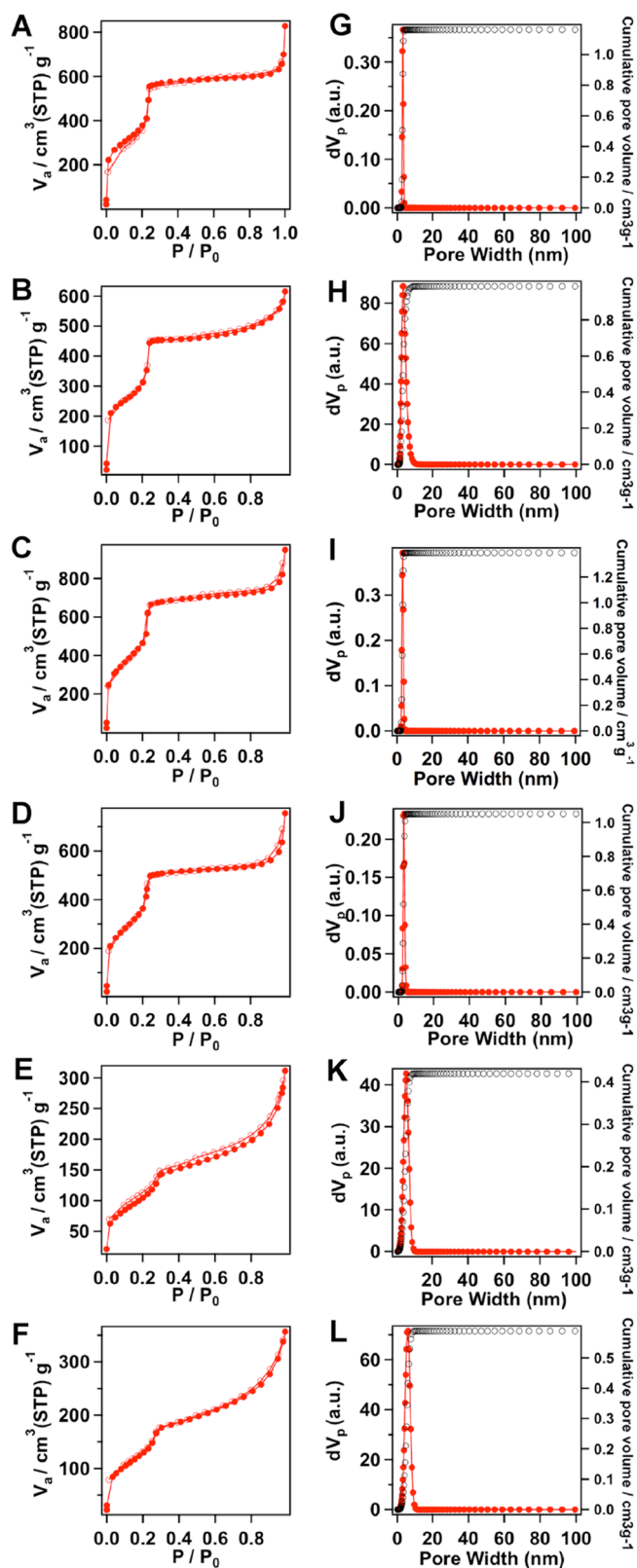
Figure 5. Nitrogen sorption isotherm profiles of (A) D_{CuPc}-A_{PyrDI}-COF, (B) D_{NiPc}-A_{PyrDI}-COF, (C) D_{CuPc}-A_{NDI}-COF, (D) D_{NiPc}-A_{NDI}-COF, (E) D_{CuPc}-A_{PDI}-COF, and (F) D_{ZnPc}-A_{PDI}-COF. Pore size distribution profiles of (G) D_{CuPc}-A_{PyrDI}-COF, (H) D_{NiPc}-A_{PyrDI}-COF, (I) D_{CuPc}-A_{NDI}-COF, (J) D_{NiPc}-A_{NDI}-COF, (K) D_{CuPc}-A_{PDI}-COF, and (L) D_{ZnPc}-A_{PDI}-COF.
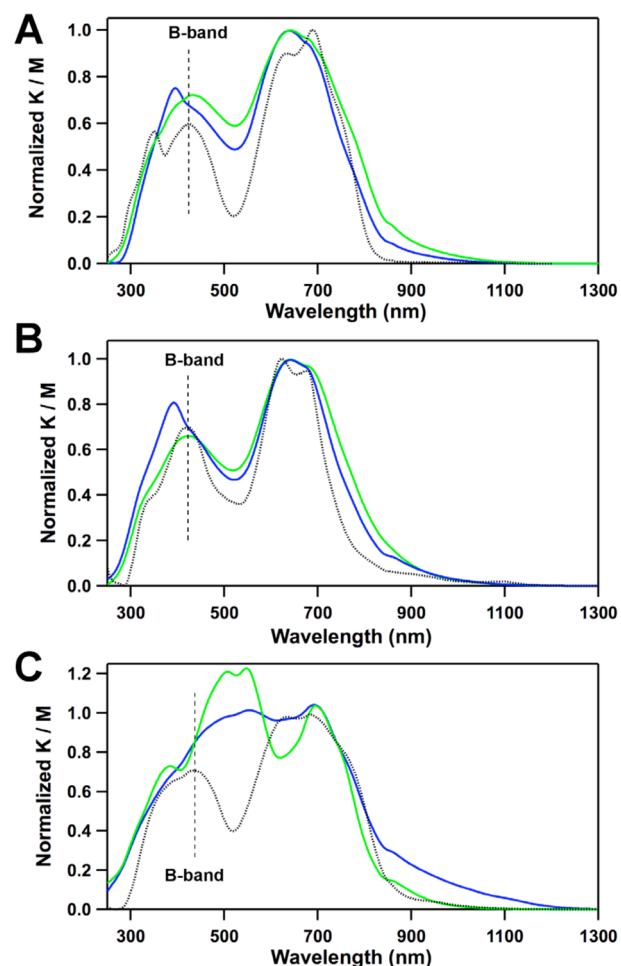
Figure 6. UV−vis spectra of (A) D_{CuPc}-A_{PyrDI}-COF (green line), D_{CuPc}-A_{NDI}-COF (blue line), and $CuPc[OMe]_8$ (dotted black line); (B) D_{NiPc}-A_{PyrDI}-COF (green line), D_{NiPc}-A_{NDI}-COF (blue line), and $NiPc[OMe]_8$ (dotted black line); and (C) D_{CuPc}-A_{PDI}-COF (blue line), D_{ZnPc}-A_{PDI}-COF (green line), and $ZnPc[OMe]_8$ (dotted black line).

COFs. For example, D_{CuPc}-A_{NDI}-COF and D_{NiPc}-A_{NDI}-COF exhibited red shifts from 386 to 395 and 392 nm, respectively. Similarly, D_{ZnPc}-A_{PDI}-COF exhibited two peaks at 506 and 549 nm, which were 10 nm red-shifted from the PDI monomers. (3) Owing to the different absorption regions of MPc and DI units (Figure S3, SI), D_{MPc}-A_{DI}-COFs broaden and enhance the light absorbance. In particular, when PDI was utilized as the counterpart that covers visible region between 380 and 610 nm with strong absorbance near 500 nm, the resulted D_{CuPc}-A_{PDI}-COF and D_{ZnPc}-A_{PDI}-COF could merge the absorbance of MPc at near-infrared region with that of PDI at visible region, allowing for a broad covering of solar spectrum. As shown in Figure 6C, D_{CuPc}-A_{PDI}-COF adsorbs a wide range of photons from visible region to near-infrared area extended to even 1200 nm. (4) The above absorption spectra features indicate that in D_{MPc}-A_{DI}-COFs, the MPc and DI units do not trigger ground-state interactions such as charge-transfer complex formation, which usually exhibits red-shifted peaks at wavelength after 1500 nm. Therefore, the electron donor and acceptor units are periodically ordered in the COFs and exist as independent π-columns, although they are covalently linked.

2.6. Structural Features of Donor−Acceptor COFs. The structural features of donor−acceptor COFs can be summar-

ized into two structural hierarchies. (1) At the primary structural level, the donor and acceptor units are covalently bonded by the boronate ester linkages and form extended 2D tetragonal polygon sheets according to the topological design diagram. Therefore, at this level, the component, the linkage, and the topology can be designed. In this study, we demonstrated metallophthalocyanine with different metal species and diimide with different π-systems as the building blocks and constructed periodically ordered donor−acceptor lattice structure. Each donor and acceptor units are interfaced to make heterojunctions in the COFs. The lattice size is determined by the donor and acceptor size, whereas the distance between the donor and acceptor is basically dependent on the lattice size. (2) At the high structural order level, the 2D sheets crystallize to form layered structures, generating periodic π-columns and 1D open nanopores (Chart 2A).

Chart 2. (A) Schematic Representation of Layered Structures of Donor−Acceptor COFs and (B) Motion of Charges in the π-Columns Leads to Two Different Lifetimes[a]
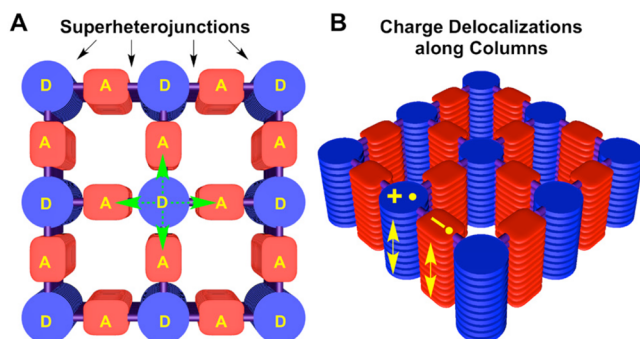
[a]In (A) each column of metallophthalocyanine donors (blue) is directly linked to four diimide acceptor columns (red). Photoinduced electron transfer has discrete columnar pairs at different distances, whereas one route is between the proximate neighboring pairs (green arrows) and another path is between the remote diagonal pairs. In (B) carrier migration along the same direction yields the short lifetime, whereas motion along opposite directions leads to long lifetime

In the columnar structure, the donor and acceptor are periodically aligned into π-arrays, whereas each donor columns are directly linked to four acceptor columns. From the photoinduced electron transfer and the charge separation perspective, the donor−acceptor COFs combine three characteristics: (1) From the heterojunction point of view, in the COFs, each donor and acceptor are molecularly interfaced to assume the largest numbers of heterojunctions for charge separation. (2) From the viewpoint of charge transport, the donor and acceptor columns offer independent pathways for exciton migration and hole and electron transports. Consequently, the molecularly interfaced superheterojunctions work synergistically for charge separation and transport. (3) From the viewpoint of photoinduced electron transfer, the donor and acceptor units are paired into two classes of π-columns with different spatial distances. One class is the four proximate pairs that are directly linked (green arrows, Chart 2A), and another class is the remote eight pairs without direct linkages. Therefore, when one donor unit is excited by light, these COFs provide four equivalent acceptors stacked in proximate columns and another eight equivalent acceptors

stacked in remote columns for accepting the electron. Therefore, the probability of charge separation is greatly enhanced. In D_{CuPc}-A_{PyrDI}-COF, D_{NiPc}-A_{PyrDI}-COF, D_{CuPc}-A_{NDI}-COF, and D_{NiPc}-A_{NDI}-COF, the proximate donor−acceptor pairs have a center-to-center distance of 1.8 nm, whereas the remote pairs have a distance of 4.0 nm. On the other hand, in D_{CuPc}-A_{PDI}-COF and D_{ZnPc}-A_{PDI}-COF, the center-to-center distances for the proximate and remote pairs are 2.0 and 4.5 nm, respectively. Therefore, the donor−acceptor D_{MPc}-A_{DI}-COFs provide clear electron-transfer pathways for charge separation; the discrete center-to-center distances allow the fine screening of donor and acceptor structures for achieving long-lived charge separation and photoenergy conversion.

From the electron-transfer distance point of view, the remote pairs are spatially separated too far to enable the photoinduced electron transfer.[15] In the proximate columnar pairs, photo-induced electron transfer generates a cation radical in the MPc column and an anion radical in the DI column. Both radical species can migrate along the columns, thus giving rise to two possibilities for the charge separation. One is that the two radicals move along the same direction and another one is along an opposite direction; the former one yields a relatively short distance between two radicals, whereas the latter one leads to a longer distance between the radical species when the charge migration proceeds (Chart 2B). Therefore, two kinds of charge-separated states would be observable in this case.

2.7. Photoinduced Electron-Transfer Dynamics. The exited states of MPcs ($^1CuPc^*$ and $^1NiPc^*$) provide sufficient driving forces for the electron transfer from $^1CuPc^*$ and $^1NiPc^*$ to the electron acceptors in the corresponding COFs upon the excitation of CuPc and NiPc at 355 nm in the polar solvents (see Table S2 and SI for the details of calculations of driven force). The photoinduced electron-transfer events were investigated by time-resolved transient absorption spectroscopy. We dispersed D_{MPc}-A_{DI}-COF samples in benzonitrile and irradiated the suspension at room temperature with nanosecond laser pulse at 355 nm. We could not directly observe the formation of the electron-transfer products of the corresponding donor and acceptor units, i.e. the radical ion pairs, in these transient absorption spectra. Instead, the transient absorption spectra of COFs (Figures 7 and S4, SI) exhibit negative absorption bands, which are the mirror image of the steady-state absorption spectra of corresponding COFs with 10−15 nm redshift (Figures 7 and S5−S8, SI). These transient traits are also different from those of the triplet excited states of monomeric $CuPc[OMe]_8$ and $NiPc[OMe]_8$ (Figures S9 and S10, SI). In addition, the triplet−triplet energy transfer from the excited MPcs to the electron acceptors is not feasible thermodyanmically.[16]

The mirror-imaged negative transient features have been previously observed in D_{ZnPc}-A_{NDI}-COF, which were interpreted as the indication of the charge delocalization along the extensive π-columns taking place after the fast photoinduced charge separation between the adjacent donor−acceptor units.[2b,17] It is important to note that the time-resolved electron spin resonance (TR-ESR) measurements confirmed the formation radical ion pair and the electron delocalization in D_{ZnPc}-A_{NDI}-COF.

The mirror-imaged negative transient absorption with a significant redshift compared to the steady-state absorption of the donor or acceptor units was regarded as the evidence of the photoinduced electron transfer in the hybrid nanostructured donor−acceptor systems. In a previous report, the charge
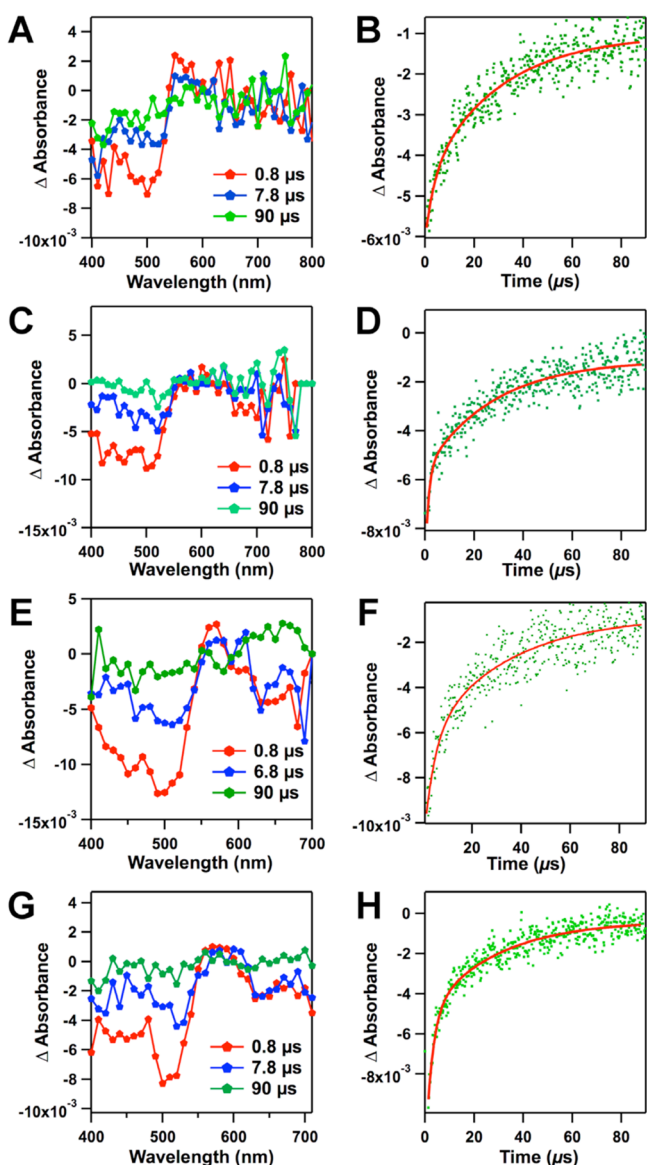
Figure 7. Transient absorption spectra of (A) D_{CuPc}-A_{PyrDI}-COF, (C) D_{NiPc}-A_{PyrDI}-COF, (E) D_{CuPc}-A_{NDI}-COF, and (G) D_{NiPc}-A_{NDI}-COF. Decay profiles of (B) D_{CuPc}-A_{PyrDI}-COF, (D) D_{NiPc}-A_{PyrDI}-COF, (F) D_{CuPc}-A_{NDI}-COF, and (H) D_{NiPc}-A_{NDI}-COF.

transient absorption minima were observed in the hybrid system of graphene-ZnPc after the photoexcitation.[20] In this hybrid system, the photoinduced charge separation was recognized by the positive trait of oxidized ZnPc at 840 nm and the bleaching of reduced graphene at 1290 nm, significantly red-shifted compared to that of the neutral graphene. In the above-mentioned hybrid systems, the molecular components (TTF, coenzyme Q10, and ZnPc), which were quite soluble in the corresponding solvents, gave positive electron-transfer characteristics in the transient spectra, whereas the dispersed or suspended nanostructure components (SWCNT and graphene) showed negative transient traits for the electron-transfer products. In this case, both of the donor and acceptor components, tightly stacked in the two-dimensionally extending COFs, are not soluble but are dispersed in the solvents. This may hinder the direct observation of the positive features of the radical ion pairs of these COFs in the transient spectra. The negative transient traits are probably a result from the delocalized states of charges following the initial, fast charge separation in the dispersed nanometer-size structures.

The immediate formation of the negative traits of COFs in the nanosecond transient absorption spectra indicates that the formation of charge migration following the initial charge separation is faster than 400 ns.[21] It also indicates that the spin state of the charge-separated state is singlet. The decay of the minima at 510 nm in the transient absorption spectra of the corresponding COF was regarded as the recombination of the migrating charges in the columns of COFs to the ground states. Thus, the overall lifetimes of the charge-separated states (τ_{CS}) via the charge migration in the π-columns can be estimated from these decays in each COFs (Figure 7). D_{CuPc}-A_{PyrDI}-COF, D_{CuPc}-A_{NDI}-COF, D_{NiPc}-A_{PyrDI}-COF, and D_{NiPc}-A_{NDI}-COF revealed two-component decays at 510 nm. The lifetime values were obtained by fitting to a sum of two decaying exponentials, i.e., τ_{CS1} and τ_{CS2} (see SI for the fitting details) and summarized in Table 2. The final lifetime values for charge separation in the D_{CuPc}-A_{DI}-COFs were relatively longer (τ_{CS2} = 33 μs) compared to those of D_{NiPc}-A_{DI}-COFs (τ_{CS2} = 26 and 29 μs for D_{NiPc}-A_{NDI}-COF and D_{NiPc}-A_{PyrDI}-COF, respectively). These results indicate that CuPc is superior to NiPc as an electron donor to form the long-lived charge-separated state, in the presence of PyrDI acceptor. On the other hand, when the donor is fixed, the τ_{CS1} and τ_{CS2} values do not change significantly between PyrDI and NDI acceptors. Only one-component decay was observed in D_{ZnPc}-A_{NDI}-COF in the previous study.[2b] The two-component decay and the difference in τ_{CS} values can be related to metal centers of the MPcs, which affect the stacking behavior of the COFs and the charge hopping dynamics in these COFs. The donor−acceptor lattice arrays in COFs achieved long-lived charge-separated states driven by charge delocalization in the columns, which suppress the charge recombination process. Besides, the lifetime values for final charge separation (τ_{CS2}) in these COFs are much longer than that observed in D_{ZnPc}-A_{NDI}-COF (Table 2). The higher oxidation states of CuPc and NiPc compared to that of ZnPc (see Table S2) may cause the charge recombination to

separation in a single-walled carbon nanotube (SWCNT) decorated with π-extended tetrathiafulvalenes (TTF) was described by the formation the positive transient traits of radical cation of TTF in the visible region and the negative imprint of the steady spectral features of SWCNT with a significant red shift compared to the van Hove singularities in the near-infrared region as result of π-electron delocalization on the SWCNT.[18] The charge separation within the SWCNT wrapped with coenzyme Q10 was also identified by the negative transient traits in the picosecond time scale, which agreed with the absolute spectrum of SWCNT.[19] Similar

Table 2. Lifetimes of Charge-Separated States of D_{MPc}-A_{DI}-COFs

		D_{CuPc}-A_{PyrDI}-COF	D_{CuPc}-A_{NDI}-COF	D_{CuPc}-A_{PDI}-COF	D_{NiPc}-A_{PyrDI}-COF	D_{NiPc}-A_{NDI}-COF	D_{ZnPc}-A_{PDI}-COF	D_{ZnPc}-A_{NDI}-COF[2b]
lifetime (μs)	τ_{CS1}	4.8	4.0	−	2.3	2.4	1.7	11
	τ_{CS2}	33	33	−	29	26	−	−

take place in the inverted region by providing much larger driving forces for back electron transfer.[22]

Along this line, we further investigated the charge separation in the COFs with the largest lattice size among the series. Because D_{CuPc}-A_{PDI}-COF and D_{ZnPc}-A_{PDI}-COF have a very poor dispersibility in solvents, the attempts using time-resolved transient absorption spectroscopy for the resolution of the photodynamics were unsuccessful. We turned to the technique of TR-ESR spectroscopy to track the formation of radical species in the solid samples of the COFs upon laser irradiation. Owing to the interference by a very strong paramagnetic signal arising from the central copper(II) species, TR-ESR spectral profile of D_{CuPc}-A_{PDI}-COF was difficult to be resolved (Figure S11, SI). In sharp contrast, D_{ZnPc}-A_{PDI}-COF after laser flash yielded a rapidly increased TR-ESR signal, which increased up to 1.35 μs and then decayed slowly (Figure 8A). Therefore, we
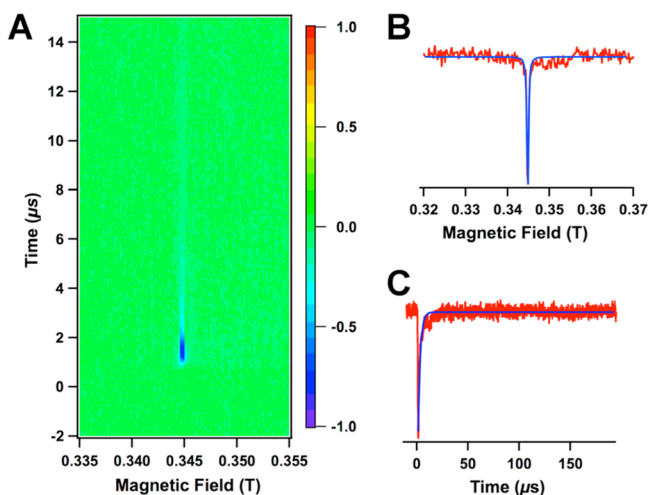
Figure 8. Contour plot of the TR-ESR spectroscopy profiles of D_{ZnPc}-A_{PDI}-COFs: (A) D_{ZnPc}-A_{PDI}-COF at 230 K; (B) magnetic field dependence profiles; and (C) time dependence profile.

monitored the TR-ESR spectra at t = 1.7 μs as a function of the magnetic field and generated a time sliced profile. This curve can be fitted with a single emission-type Lorentzian with a g value of 2.0043 and a narrow spectra width of 0.41 mT (Figure 8B). This g value confirms the formation of $ZnPc^{\bullet+}$ and $PDI^{\bullet-}$ species.[23] The narrow spectral width is consistent with a weak magnetic dipolar interaction between two spins, which are separated and delocalized in spatially separated and independent π columns. Through the curve fitting of the time profiles to an exponential function given by $\Phi = \alpha \exp[-t/\tau_{CS}]$, where α, t, and τ_{CS} are the proportional factor, time, and lifetime, respectively, the τ_{CS} value was evaluated to be 1.7 μs at 230 K (Figure 8C). The lifetime of charge-separated state in the largest lattice COF is still at the same level among the COF series, which means that the lattice size does not affect the charge separation significantly and thus indicates that such a donor−acceptor system is quite applicable with different components.

3. CONCLUSIONS

Through the systematic study on the synthesis, structural resolution, and photochemical events, we demonstrated that donor−acceptor COFs can be a powerful platform for constructing segregated bicontinuous superheterojunctions for photoinduced electron transfer and charge separation via direct

polycondensation under solvothermal conditions. The topological diagram directs the formation of tetragonal lattice with donor at the vertices and acceptor on the edges, whereas the extended 2D polygon sheets crystallize to generate layered frameworks. From a synthetic point of view, a significant feature is that this methodology enables the covalent integration of metallophthalocyanines and diimides, irrespective of their central metal species and π-systems, into a similar lattice structure. Therefore, the COFs offer a powerful platform for synthesizing predesigned periodic arrays of donor and acceptor columns, which have been hardly achieved by using other covalent or noncovalent approaches.

Each metallophthalocyanine donor and diimide acceptor units in the COFs are interfaced, thus giving rise to periodically ordered molecular heterojunctions. Such a structure thus constitutes exceptional area of interface for charge separation, a key issue to be solved in the current organic and polymeric solar cells. The periodic arrays of metallophthalocyanine donor and diimide acceptor columns not only provide discrete donor−acceptor pairs for photoinduced electron transfer and charge separation but also offer predesigned pathways for charge transport and collection. These structural features and functions of the donor−acceptor COFs demonstrate a photoactive structure with an ideal mechanism for charge separation and collection in solar cells.

Time-resolved spectroscopy revealed that the donor−acceptor COFs are capable of electron transfer with long-lived charge separation. The periodically ordered columnar arrays play an important role in enhancing the lifetime of charge-separated state, as a result of charge carrier migration. These long-lived charge separation states offer the great chance to extract holes and electrons for electric current production. In short, the structural features of the donor−acceptor COFs and insights into the mechanistic aspects of charge separation constitute a basis for developing COFs in photovoltaic applications.

■ ASSOCIATED CONTENT

Ⓢ Supporting Information

Materials and methods, synthetic protocols, and spectral profiles. The Supporting Information is available free of charge on the ACS Publications website at DOI: 10.1021/jacs.5b03553.

■ AUTHOR INFORMATION

Corresponding Authors

*sirle@chem.nagoya-u.ac.jp
*fukuzumi@chem.eng.osaka-u.ac.jp
*jiang@ims.ac.jp

Notes

The authors declare no competing financial interest.

■ ACKNOWLEDGMENTS

■ REFERENCES

(1) Feng, X.; Ding, X.; Jiang, D. *Chem. Soc. Rev.* **2012**, *41*, 6010−6022.

(2) (a) Feng, X.; Chen, L.; Honsho, Y.; Saengsawang, O.; Liu, L.; Wang, L.; Saeki, A.; Irle, S.; Seki, S.; Dong, Y. P.; Jiang, D. *Adv. Mater.* **2012**, *24*, 3026−3031. (b) Jin, S.; Ding, X.; Feng, X.; Supur, M.; Furukawa, K.; Takahashi, S.; Addicoat, M.; El-Khouly, E. M.;

Nakamura, T.; Irle, S.; Fukuzumi, S.; Nagai, A.; Jiang, D. *Angew. Chem., Int. Ed.* **2013**, *52*, 2017−2021. (c) Jin, S.; Furukawa, K.; Addicoat, M.; Chen, L.; Takahashi, S.; Irle, S.; Nakamura, T.; Jiang, D. *Chem. Sci.* **2013**, *4*, 4505−4511.

(3) (a) Côté, A. P.; Benin, A.; Ockwig, N.; O'Keeffe, M.; Matzger, A.; Yaghi, O. M. *Science* **2005**, *310*, 1166−1170. (b) Côté, A. P.; El-Kaderi, H. M.; Furukawa, H.; Hunt, J. R.; Yaghi, O. M. *J. Am. Chem. Soc.* **2007**, *129*, 12914−12915.

(4) Tilford, R. W.; Gemmill, W. R.; zur Loye, H. C.; Lavigne, J. J. *Chem. Mater.* **2006**, *18*, 5296−5301.

(5) (a) Nagai, A.; Guo, Z.; Feng, X.; Jin, S.; Chen, X.; Ding, X.; Jiang, D. *Nat. Commun.* **2011**, *2*, 536 DOI: 10.1038/ncomms1542. (b) Wan, S.; Guo, J.; Kim, J.; Ihee, H.; Jiang, D. *Angew. Chem., Int. Ed.* **2008**, *47*, 8826−8830. (c) Wan, S.; Guo, J.; Kim, J.; Ihee, H.; Jiang, D. *Angew. Chem., Int. Ed.* **2009**, *48*, 5439−5442. (d) Ding, X.; Guo, J.; Feng, X.; Honsho, Y.; Guo, J. D.; Seki, S.; Maitarad, P.; Saeki, A.; Nagase, S.; Jiang, D. *Angew. Chem., Int. Ed.* **2011**, *50*, 1289−1293. (e) Ding, X.; Chen, L.; Honso, Y.; Feng, X.; Saengsawang, O.; Guo, J. D.; Saeki, A.; Seki, S.; Irle, S.; Nagase, S.; Parasuk, V.; Jiang, D. *J. Am. Chem. Soc.* **2011**, *133*, 14510−14513. (f) Feng, X.; Chen, L.; Dong, Y. P.; Jiang, D. *Chem. Commun.* **2011**, *47*, 1979−1981. (g) Feng, X.; Liu, L.; Honsho, Y.; Saeki, A.; Seki, S.; Irle, S.; Dong, Y. P.; Nagai, A.; Jiang, D. *Angew. Chem., Int. Ed.* **2012**, *51*, 2618−2622. (h) Ding, X.; Feng, X.; Saeki, A.; Seki, S.; Nagai, A.; Jiang, D. *Chem. Commun.* **2012**, *48*, 8952−8954. (i) Feng, X.; Dong, Y. P.; Jiang, D. *CrystEngComm.* **2013**, *15*, 1508−1511. (j) Chen, X.; Addicoat, M.; Irle, S.; Nagai, A.; Jiang, D. *J. Am. Chem. Soc.* **2013**, *135*, 546−549. (k) Guo, J.; Xu, Y.; Jin, S.; Chen, L.; Kaji, T.; Honsho, Y.; Addicoat, M.; Kim, J.; Saeki, A.; Ihee, H.; Seki, S.; Irle, S.; Hiramoto, M.; Gao, J.; Jiang, D. *Nat. Commun.* **2013**, *4*, 2736. (l) Xu, H.; Chen, X.; Gao, J.; Lin, J.; Addicoat, M.; Irle, S.; Jiang, D. *Chem. Commun.* **2014**, *50*, 1292−1294. (j) Huang, N.; Chen, X.; Krishna, R.; Jiang, D. *Angew. Chem., Int. Ed.* **2015**, *54*, 2986−2990.

(6) (a) Dogru, M.; Handloser, M.; Auras, F.; Kunz, T.; Medina, D.; Hartschuh, A.; Knochel, P.; Bein, T. *Angew. Chem., Int. Ed.* **2013**, *52*, 2920−2924. (b) Calik, M.; Auras, F.; Salonen, L. M.; Bader, K.; Grill, I.; Handloser, M.; Medina, D. D.; Dogru, M.; Löbermann, F.; Trauner, D.; Hartschuh, A.; Bein, T. *J. Am. Chem. Soc.* **2014**, *136*, 17802−17807. (c) Medina, D. D.; Rotter, J. M.; Hu, Y.; Dogru, M.; Werner, V.; Auras, F.; Markiewicz, J. T.; Knochel, P.; Bein, T. *J. Am. Chem. Soc.* **2015**, *137*, 1016−1019.

(7) Patwardhan, S.; Kocherzhenko, A. A.; Grozema, F. C.; Siebbeles, L. D. A. *J. Phys. Chem. C* **2011**, *115*, 11768−11772.

(8) (a) Spitler, E. L.; Dichtel, W. R. *Nat. Chem.* **2010**, *2*, 672−677. (b) Colson, J. W.; Woll, A. R.; Mukherjee, A.; Levendorf, M. P.; Spitler, E. L.; Shields, V. B.; Spencer, M. G.; Park, J.; Dichtel, W. R. *Science* **2011**, *332*, 228−231. (c) Spitler, E. L.; Colson, J. W.; Uribe-Romo, F. J.; Woll, A. R.; Glovino, M. R.; Saldivar, A.; Dichtel, W. R. *Angew. Chem., Int. Ed.* **2012**, *51*, 2623−2627.

(9) Lukose, B.; Kuc, A.; Heine, T. *Chem. —Eur. J.* **2011**, *17*, 2388−2392.

(10) Kuhn, P.; Antonietti, M.; Thomas, A. *Angew. Chem., Int. Ed.* **2008**, *47*, 3450−3453.

(11) Campbell, N. L.; Clowes, R.; Ritchie, L. K.; Cooper, A. I. *Chem. Mater.* **2009**, *21*, 204−206.

(12) Berlanga, I.; Ruiz-González, M. L.; González-Calbet, J. M.; Fierro, J. L. G.; Mas-Ballesté, R.; Zamora, F. *Small* **2011**, *7*, 1207−1211.

(13) (a) Li, W.; Yamamoto, Y.; Fukushima, T.; Saeki, A.; Seki, S.; Tagawa, S.; Masunaga, H.; Sasaki, S.; Takata, M.; Aida, T. *J. Am. Chem. Soc.* **2008**, *130*, 8886−8887. (b) Kira, A.; Umeyama, T.; Matano, Y.; Yoshida, K.; Isoda, S.; Park, J. K.; Kim, D.; Imahori, H. *J. Am. Chem. Soc.* **2009**, *131*, 3198−3200. (c) Hayashi, H.; Nihashi, W.; Umeyama, T.; Matano, Y.; Seki, S.; Shimizu, Y.; Imahori, H. *J. Am. Chem. Soc.* **2011**, *130*, 10736−10739. (d) Tu, S.; Kim, S. H.; Joseph, J.; Modarell, D. A.; Parquette, J. R. *J. Am. Chem. Soc.* **2011**, *133*, 19125−19130. (e) Ley, D.; Guzuman, C. X.; Adolfsson, K. H.; Scott, A. M.; Braunschweig, A. B. *J. Am. Chem. Soc.* **2014**, *136*, 7809−7812. (f) Hartnett, R. E.; Dyar, S. M.; Margulies, E. A.; Shoer, L. E.; Cook, A.

W.; Eaton, S. W.; Marks, T. J.; Wasielewski, M. R. *Chem. Sci.* **2015**, *6*, 402−411. (g) Rao, K. V.; Haldar, R.; Kulkarni, C.; Maji, T. K.; Gerorge, S. J. *Chem. Mater.* **2012**, *24*, 969−971. (h) Rao, K. V.; Mohapatra, S.; Maji, T. K.; Geroge, S. J. *Chem. —Eur. J.* **2012**, *18*, 4504−4509.

(14) Kasha, M.; Rawls, H. R.; Ashraf El-Bayoumi, M. *Pure Appl. Chem.* **1965**, *11*, 371−392.

(15) Ramamurthy, V.; Schanze, K. S. *Organic and Inorganic Photochemistry*; Marcel Dekker: New York, 1998.

(16) Supur, M.; El-Khouly, M. E.; Seok, J. H.; Kay, K.-Y.; Fukuzumi, S. *J. Phys. Chem. A* **2011**, *115*, 14430−14437.

(17) In the previous report, we could observe the fast formation of the radical ion pair in the picosecond time scale when the solubility of the D_{ZnPc}-A_{NDI}-COF was improved by delamination. In this case, the dispersion of the COFs was relatively low in many common organic solvents.

(18) Herranz, M. A.; Ehli, C.; Campidelli, S.; Gutierrez, M.; Hug, G. L.; Ohkubo, K.; Fukuzumi, S.; Prato, M.; Martin, N.; Guldi, D. M. *J. Am. Chem. Soc.* **2008**, *130*, 66−73.

(19) Ohtani, M.; Fukuzumi, S. *Chem. Commun.* **2009**, 4997−4999.

(20) Malig, J.; Jux, N.; Kiessling, D.; Cid, J. J.; Vazquez, P.; Torres, T.; Guldi, D. M. *Angew. Chem., Int. Ed.* **2011**, *50*, 3561−3565.

(21) The detector of our nanosecond laser system cannot detect the photoinduced events faster than 400 ns.

(22) (a) Marcus, R. A.; Sutin, N. *Biochim. Biophys. Acta* **1985**, *811*, 265−322. (b) Marcus, R. A. *Pure Appl. Chem.* **1997**, *69*, 13−29.

(23) Nkyokong, T.; Gasyma, Z.; Stillman, M. J. *Inorg. Chem.* **1987**, *26*, 548−553.